



# Effect of Pt/TiO<sub>2</sub> interface on room temperature hydrogen sensing performance of memristor type Pt/TiO<sub>2</sub>/Pt structure



Azhar Ali Haidry<sup>a,b,\*</sup>, Andrea Ebach-Stahl<sup>a</sup>, Bilge Saruhan<sup>a</sup>

<sup>a</sup> Institute of Materials Research, German Aerospace Center (DLR), Linder Hoehe, 51147 Cologne, Germany

<sup>b</sup> College of Materials Science and Technology (MST), Nanjing University of Aeronautics and Astronautics (NUAA), Jiangjun Avenue 29, Nanjing 21101, PR China

## ARTICLE INFO

### Article history:

Received 18 March 2017

Received in revised form 18 May 2017

Accepted 23 June 2017

Available online 1 July 2017

### Keywords:

Hydrogen sensors

Pt/TiO<sub>2</sub>/Pt

Memristor

Metal/Semiconductor interface

Conducting filaments

## ABSTRACT

In this paper, a sensor with memristor electrode geometry (Pt/TiO<sub>2</sub>/Pt) was fabricated by a simple and cost-effective method yielding 10<sup>6</sup> orders of resistance change with short reaction times ( $T_{res} \sim 19$  and  $T_{rec} \sim 118$  s) when exposed to 1 vol.% H<sub>2</sub>. Under wet conditions an increase in sensor response toward 1 vol.% H<sub>2</sub> independent of operating temperature RT–100 °C ( $T_{res} \sim 5$  s) and a reasonable H<sub>2</sub>-selectivity was observed in the presence of CO and NO<sub>2</sub>. Such sensor characteristics with lower power consumption offer great advantages and are highly suitable for fuel cell and hydrogen safety applications. Despite the knowledge that hydrogen atoms accumulate at Pt/TiO<sub>2</sub> interface reducing Schottky barrier height (i.e. decreasing the resistance of the Pt/TiO<sub>2</sub> interface by several orders of magnitude) the details of the involved sensing mechanisms, especially under humidity, is still incomplete. The results confirm the existence of both electronic and ionic conductivity within TiO<sub>2</sub> sensing layer and their significant alteration under hydrogen exposure. Thus a sensing model is proposed that fit exceptionally well with the memristor-type resistance variation principle. The understanding gained by the proposed model will allow the fabrication of innovative sensors for stable, selective and robust H<sub>2</sub> detection.

© 2017 Elsevier B.V. All rights reserved.

## 1. Introduction

Undoubtedly hydrogen (H<sub>2</sub>) is meticulously regarded as the future green energy carrier due to its harmless by-product, water. Despite being the lightest element on the periodic table, as an energy carrier, hydrogen has been utilized in many applications including aerospace, automotive, photochemical, transport and power generation. With authenticating the opening of world's first tri-generation fuel cell and hydrogen station, the demand of hydrogen carried energy is expected to increase rapidly [1–3]. However, there are rising concerns over the safe use, storage and transport of hydrogen as an energy carrier because H<sub>2</sub> is colorless and odorless but in air is flammable at low concentrations (4 vol.%) with very low ignition energy and combusts in air [4]. The sensing characteristics of hydrogen gas sensors can be significantly altered when the operating environment changes; i.e. temperature and humid-

ity. Therefore, it is crucial to develop a new class of cost-effective, reliable, robust and accurate sensing systems to facilitate early detection of H<sub>2</sub> before the gas concentrations rise to hazardous levels [4–6].

Despite being small in size and cost-effective, the most successful commercial sensors based on metal oxides require a significant pre-heating of the sensing element (up to 300–700 °C) to achieve the desired sensitivity and accuracy. In order to avoid instability, to increase robustness and to enable lower operational costs with a significantly longer operational lifetime, H<sub>2</sub> gas sensors should consume little power, be inexpensive, and easy to integrate with existing monitoring systems, properties that could be realized while operating at room temperature. The sensors based on nanomaterials (nanotubes, nanowires, nanobelts etc.) work well even at room temperature [7,8] but their fabrication requires sophisticated as well as expensive equipment, thus increasing the production costs. The common application is to use metallic circuits (or electrodes), mostly with interdigitated structures (designated as IDEs). Since the distance between the electrodes within the IDE is in the order tens of microns to tens of millimeters, added with the very low conductivity of the MOX sensing layer, it is difficult to get any reasonable sensor signal (resistance change  $\sim \Delta R = R_{air}/R_{gas}$ ) for standard n-type semiconductor at room temperature.

\* Corresponding author. Present address: College of Materials Science and Technology (MST), Nanjing University of Aeronautics and Astronautics (NUAA), Jiangjun Avenue 29, Nanjing 21101, PR China. Tel.: +8615895837907, +4922036013228; fax: +492203696480.

E-mail addresses: [baa.haidry@nuaa.edu.cn](mailto:baa.haidry@nuaa.edu.cn), [azharalig2@gmail.com](mailto:azharalig2@gmail.com) (A.A. Haidry).

The Pt/TiO<sub>2</sub>/Pt (Metal/Oxide/Metal – MOM) structures are mostly utilized in Memristor's fabrication. In comparison to other metallic electrodes (Au, Ag, Cu and Al), Pt is preferred due to its high melting point (~1772 °C), excellent adhesion with the variety of substrates, high chemical, physical and electrical stability. Pt can withstand and does not oxidize under high-temperature annealing conditions: a necessary step to achieve crystalline TiO<sub>2</sub> films and reduced Pt/TiO<sub>2</sub> Schottky interface. Moreover, for hydrogen sensors, it is proven that Pt acts as a catalyst to dissociate hydrogen molecules that can migrate quickly to the TiO<sub>2</sub> surface and further diffuse into the bulk. Therefore the role of Pt electrode is important in terms of sensing mechanism and is discussed later in detail (see the Section 4.4). Recently, some reports pointed out the potential of Pt/TiO<sub>2</sub>/Pt structures for use in gas sensors, particularly for detection of hydrogen at room temperature with the semiconducting oxide sensor materials by eliminating the otherwise required heating [9–11]. The report [9] discussed that, in the sensor design, the reduction of the top electrode dimension to nanoscale (below 100 nm) enables a high sensitivity enhancement toward 10000 ppm H<sub>2</sub> at room temperature. However, it was assumed that the Schottky barrier height at both top and bottom electrode interfaces is same for such electrode dimension. Moreover, low H<sub>2</sub> concentration threshold, the influences of humidity on sensing, selectivity and operation temperature was not considered in this report.

In this context, the present report elucidates the influence of metal/semiconductor interface, background humidity and operating temperature related conditions on respective electrical transport characteristics and gas sensing mechanism of these structures without going into any nanoscale changes in the sensor design dimensions. Therefore, the novelty of this report is to establish a respective sensing mechanism for this sensor design by investigating the role of such effects on hydrogen gas sensitivity performance at the temperature range between 24° (RT) to 100 °C and under 50% RH. At room temperature, the prepared samples demonstrated five orders of magnitude resistance change in dry air and enhanced hydrogen sensing properties under 50% humidity with negligible operating temperature effect up to 100 °C. On the basis of these analyses, a novel hydrogen sensing mechanism is proposed, which involves the formation of “ionic conduction channel” due to the drift of ions (mainly oxygen vacancies) from one electrode to other depending on biasing condition. According to this model, during adsorption/desorption of hydrogen gas on the surface, the width of this conduction channel changes drastically, thus, as a consequence, very small changes in the resistance can be detected. These analysis and sensing mechanism adds an in-depth scientific contribution to the current sensing model concerning relatively low-level hydrogen exposure at room temperature.

## 2. Construction of the sensors

The Pt/TiO<sub>2</sub>/Pt sensors were prepared on as received polished polycrystalline alumina substrates (from Siebert Thin Film Technology GmbH, Hermsdorf, Germany). Both bottom (TE) and top (BE) Pt electrodes were fabricated through an in-house laser patterned mask prepared from a Ferrum plate without applying any secondary adhesive layer or lift-off technique by sputter deposition of Pt target (99.99% purity) in SCD 500 Sputter Coater from BAL-TEC Germany. The sputtering lasted 2 min under a chamber pressure of  $<1 \times 10^{-1}$  resulting in ~200 nm thickness at both Pt-BE and Pt-TE. The TiO<sub>2</sub>-sensing layers (SL) were prepared by reactive magnetron sputtering from Ti-targets in Ar + O<sub>2</sub> atmosphere as described elsewhere in details [10]. Briefly summarized, a sputtering power of 800 W was applied on Ti-target under argon and oxygen flow for 8 h yielding TiO<sub>2</sub>-sensing layer with a nominal 2 μm thickness. No

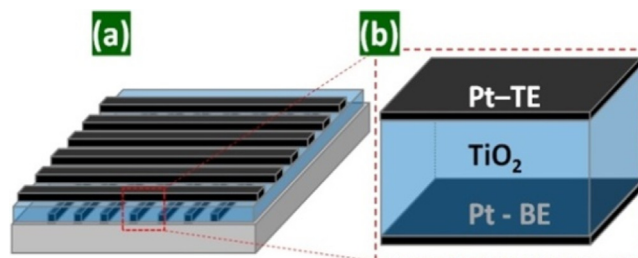


**Fig. 1.** The schematics of final Al<sub>2</sub>O<sub>3</sub>/Pt/TiO<sub>2</sub>/Pt sensor structure: The process steps involved in the fabrication of Pt/TiO<sub>2</sub>/Pt sensor structures, the structuring of bottom Pt electrode Pt-BE, 2 μm thick TiO<sub>2</sub> sensing layer and top Pt electrode Pt-TE having the same dimension as Pt-BE respectively.

substrate heating was applied. These fabrication steps are shown in Fig. 1. After deposition Pt/TiO<sub>2</sub>/Pt sensing structures, the sensor samples were annealed in static air at temperatures 600 °C and 800 °C for 3 h with a heating rate of 100 °C/15 min in a muffle furnace from Heraeus Instruments. The samples annealed at 600 °C and 800 °C are labelled as T600 and T800, respectively.

## 3. Experimental

The structural investigation of the sensing layer was performed by using a SIEMENS D5000 X-ray diffractometer (XRD) in standard Bragg-Brentano geometry with a CuKα radiation ( $\lambda_{\text{CuK}\alpha} = 0.15418$  nm) and the graphite curved monochromator. For phase analysis  $\theta/2\theta$  spectra were measured in the range of  $2\theta = 23\text{--}87^\circ$  and subsequently compared with the nominal bulk data using Siemens/Bruker AXS Diffrac EVA-V3 software.

The cross-sections of the sensing layers were investigated by field effect scanning electron microscope (FE-SEM, Ultra 55 from Zeiss, Germany) equipped with built-in energy dispersive spectrometer (EDS) having an X-Ray Fluorescence Analyzer MESA 500 from Oxford Instruments. Initially, the samples were prepared carefully by standard metallographic methods in three steps; i. cutting, ii. embedding in a conductive phenolic compound, and iii. polishing with a diamond spray and a colloidal SiO<sub>2</sub> suspension. The samples were thereafter thoroughly cleaned with soap and water and dried at 100 °C overnight in an oven before the analysis. The samples were first coated with very thin (a few nm) conductive Pt layer in a Sputter Coater SCD 500 from BAL-TEC Germany. Micrographs in secondary electron and/or in lens mode were taken by applying an acceleration voltage of 3 kV and working distance of less than 5 mm. For the EDS analysis the acceleration voltage was 15 kV with a working distance of 8.5 mm.

The coating composition and depth profiles were examined with glow discharge optical emission spectrometer (GDOES) with GDA 650 equipped with CCD detector from Spectruma Analytic GmbH, Hof, Germany. A 0.5 kHz pulsed high frequency (HF) mode was applied with 650 V, a gas pressure of 2.5 hPa, duty cycle of 40%, and integration time of 200 ms. For analysis Ti, Pt and O, the corresponding atomic lines at 399 nm, 266 nm and 130 nm were used, respectively. Due to low intensity of the only available oxygen line at 130 nm a GDA 650 spectrometer (Spectruma Analytic GmbH) with a more sensitive detector in particular a photomultiplier was used for quantification of oxide layers on the oxidized samples. The sputtering method was HF with 500 V and 2.5 hPa. Variations in the crater shape associated with preferential sputtering of elements can influence the GDOES profiles, especially after long sputtering times, and therefore, the measured chemical composition of the coatings. However, such changes in the crater topography were not observed as confirmed by SEM examination of the crater bottom.

The gas sensing tests of Pt/TiO<sub>2</sub>/Pt structured sensors were performed with a computer-controlled experimental setup (sensor

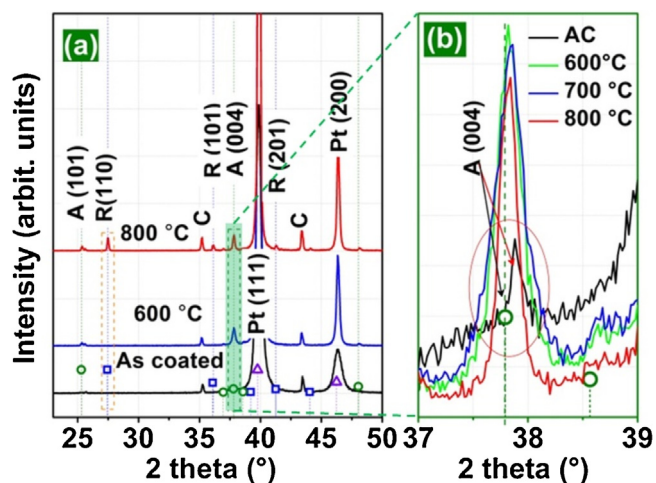


**Fig. 2.** The XRD diffractograms of as-coated (AC) and annealed samples are shown in (a), and zoomed A (004) peak shown in (b). The XRD diffractograms were compared with JCPDS (Joint Committee on Powder Diffraction Standards) card numbers 04-0802 (platinum with cubic symmetry of space group  $Fm\bar{3}m$  with  $a = 3.9231$  Å), 21-1272 (anatase with tetragonal symmetry of space group  $I4_1/amd$  with lattice constants  $a = b = 3.78$  Å and  $c = 9.522$  Å) and 21-1276 (rutile with tetragonal symmetry of space group  $P4_2/mnm$  with  $a = b = 4.5933$  Å,  $c = 2.9592$  Å).

and catalyst characterization unit – SESAM) at DLR Cologne. All the included instruments were controlled with LabVIEW program. The flow controller from MKS Instruments GmbH (MFC-647b) enables to control eight channels simultaneously. The gases flow to the gas mixing chamber and then to CARBOLITE tube furnace consisted of a Quartz-glass recipient and Keithley 2635A Source meter DC-measurement unit. In order to ensure a good electrical contact between the Pt electrodes of the sample and low noise triaxial cable (Model 237-TRX-NG) of Keithley source meter, thin Pt wires and silver paste solder were used. The setup allows measuring very high resistance (up to  $\sim 10^{11}$  ohm) with low noise and the changes in resistance, current or voltage of the sample. The gas sensing tests were performed in technical air flow at a rate of 400 ml/min with a constant 1 V bias. The test gas ( $H_2$ ) concentrations were varied in the range of 150–10000 ppm in dry and humid background technical air. The gas sensor test experimental setup is ascribed detailed in [12].

## 4. Results and discussion

### 4.1. Phase and crystal structure

Generally, the as-coated reactively sputtered  $TiO_2$  layers are amorphous in nature and crystallize to anatase on heat treatment in the temperature range of 300 °C and 600 °C transforming to rutile phase above 500 °C depending on deposition parameters, annealing conditions and substrate material [13].

Fig. 2a gives the comparative XRD diffractograms of the Pt/ $TiO_2$ /Pt/ $Al_2O_3$  structures annealed at 600 °C (T600) and 800 °C (T800). The diffraction pattern from T600 sample exhibits that the (004) peak of anatase (A) phase dominates over the low intensity peak from the A (101) plane at  $2\theta \sim 25.30^\circ$ . While at the diffraction pattern of T800 sample, also the reflection corresponding to rutile R (101) plane at  $27.44^\circ$  is visible. As Fig. 2b displays, the diffraction pattern of the as-coated Pt/ $TiO_2$ /Pt/ $Al_2O_3$  sample contains an unexpected presence of A (004) peak belonging to the anatase phase indicating a slight shift to the right (i.e. to higher  $2\theta \sim 37.88^\circ$ ). This XRD investigation reveals that the anatase phase is preferentially orientated at A (004) plane along the (111) plane of Pt and grows displaying a prolonged c-axis orientation because of epitaxial force between  $TiO_2$  and Pt (111). The appearance of a stronger A (004)

peak instead of A (100) peak (commonly observed for bulk powders) also suggests a near epitaxial growth of  $TiO_2$  on Pt (111) surface [14]. Moreover, the grain size ( $D_g$ ) at A (004) in the as-coated  $TiO_2$  is about 67 nm, calculated using the standard Scherrer formula [13]. The anatase grain size  $D_{g,a}$  calculated for both annealed samples is about  $\sim 40$  nm at A (004) and about 50 nm at A (100). Whereas the grain size of rutile  $D_{g,r}$  only for the T800 is about  $\sim 130$  nm at R (101). For the quantitative analysis, the rutile weight fraction  $W_R(\%)$  was calculated by Spurr-Mayer's equation as described in [15]. The estimated  $W_R(\%)$  of rutile phase for T800 (deposited on alumina) is 44 wt.%, while for the T800 samples deposited on single crystal sapphire substrate, the rutile weight fraction  $W_R(\%)$  was found only about 20 wt.% (see Fig. S1 of Supplementary Data – SD). The discrepancies in  $W_R(\%)$  contents indicate that the substrate material (i.e. only c-cut  $Al_2O_3$  vs Pt/polycrystalline  $Al_2O_3$ ) influences the promotion of crystallization or conversion of  $TiO_2$  even though deposition took place in the same processing run. Moreover, the relatively weak intensity of reflections from anatase/rutile phases of  $TiO_2$ , being absorbed and saturated by the strong peak from Pt (111) and corundum (indicated by “C” in Fig. 2a), results in an approximate error of 10% at calculated wt.% of rutile and anatase.

### 4.2. Microstructure and compositional analyses by FE-SEM/EDX and GDOES

As a common practice, metallic (Pt, Au, Pd, Ag etc.) electrodes are fabricated to measure the electrical resistance of the resistive-based gas sensor, such electrodes play key roles in the sensing as well as the transducing function of a sensor. In the present case, metallic platinum (Pt) based electrodes were prepared on alumina substrates owing to the excellent adhesion (with alumina substrate), chemical and thermal stability, high resistance to oxidation and high melting point of Pt. Prior to the preparation of real sensors with TBE configuration, intensive experimental work has been performed, to investigate the effect of annealing temperature on Pt and to determine the optimum fabrication parameters which are mentioned in Section 2. These parameters yielded  $\sim 200$  nm thick Pt amorphous layers (as deposited case) on both BE and TE. The surface and cross-sectional micrographs of both Pt electrodes are shown in Fig. S2 of SD. The Pt BE and TE layers showed different surface morphologies due to different underlying material types (Alumina for BE and sputtered  $TiO_2$  layer for TE). It is known that Pt has the ability to evolve its microstructure according to the crystal structure and lattice orientation of the substrate material [14].

After annealing of the sandwiched layers in static air, there was no visible change in the physical appearance of Pt electrodes at both annealed samples; T600 and T800. However, closer investigation revealed that the Pt layers of T800 samples were densely packed and had larger crystal sizes as those being vice versa for T600 samples. Further increase of the annealing temperature (900 °C or 1000 °C) resulted in the total loss of Pt layer yielding a vermicular-shaped microstructure (not shown here). Since Pt has high atom mobility, the annealing-induced changes in the microstructure of Pt layers are most likely caused by intrinsic stress and enhanced rate of surface diffusion. A thorough investigation of annealed Pt TBE has been reported in a previous report elsewhere [12].

The FE-SEM micrographs of the as-deposited  $TiO_2$  sensing layer exhibit a periodically repeating and vertically aligned micro-columnar morphology with a typical thickness of  $\sim 2$   $\mu m$  (Fig. 3a,b,c). The microcolumns consist of very fine grains which vary in the range of tens of nanometers. Column surfaces result occasionally in the occurrence of micro-textured bumps/nodes in the sizes ranging from 1 to 2  $\mu m$ . The micrographs of the heat-treated samples T600 (Fig. 3b) and T800 (Fig. 3c) in turn display large and faceted grains caused by transformation from amorphous to crystalline phase. An open and packed granular structure with

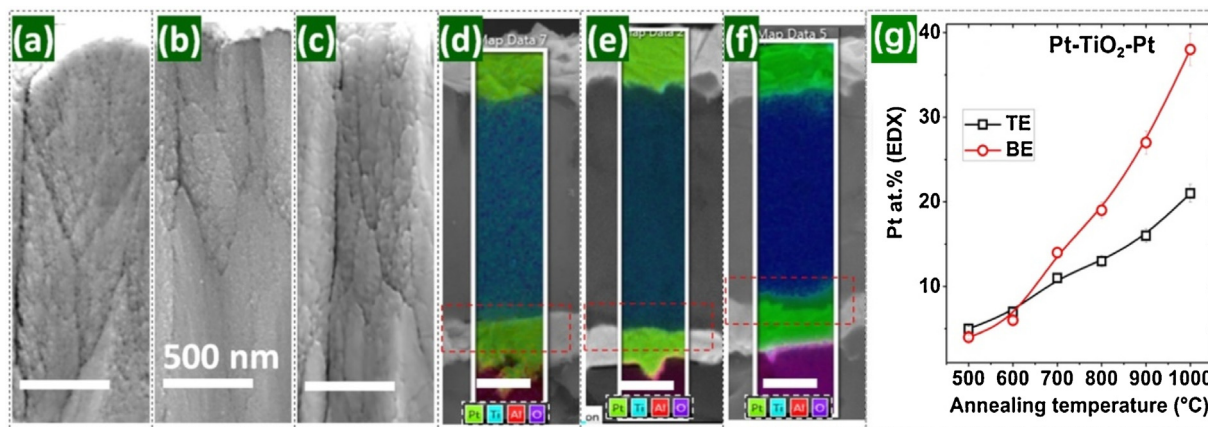


**Fig. 3.** The FE-SEM and EDS analysis of Pt/TiO<sub>2</sub>/Pt structures. The FE-SEM micrographs and EDX elemental mapping of as coated (a,d), T600 (b,e) and T800 (c,f) samples. Solid white lines in a–f indicate the 500 nm scale bar in FE-SEM micrographs. The EDX analysis of top Pt electrode (Pt-TE) and bottom Pt electrode (Pt-BE) showing the effect of annealing temperature on Pt diffusion at both interfaces (g), the approximation of Pt at.% was performed by point analysis as described in the supplementary data (S3–SD).

distinct columns and grain boundaries (voids) grows from bottom Pt layer to the sensing layer surface of the T800 sample. This may occur either due to the thermal diffusion processes during annealing or due to the movement and position adjustment of oxygen vacancies in TiO<sub>2</sub> lattice. In contrast to highly under-stoichiometric order of the as coated sample (Fig. 3d), the EDX analysis and elemental mapping at the cross-sections of T600 samples (prepared with standard metallographic methods) show a TiO<sub>2</sub> composition near to stoichiometry (Fig. 3e) with non-stoichiometric TiO<sub>2-x</sub> at the Pt-BE. Furthermore, it is noticeable for the T800 samples (Fig. 3f) that Pt diffuses into TiO<sub>2</sub> layer in a depth of a few nanometers (Fig. 3f) which may be caused by thermally induced interdiffusion at 800 °C. Approximate at.% of Pt is estimated at both interfaces by point analyses on each interface (Fig. 3g), for further details of this procedure see supplementary data: S3–SD. This analysis confirms that the diffusion rate of Pt is higher at the bottom electrode (BE) than the top electrode (TE). However, these analyses are only qualitative and give solely comparative insight about the Pt diffusion characteristics of both interfaces (i.e. Pt/TiO<sub>2</sub> and TiO<sub>2</sub>/Pt) at higher temperatures (e.g. at 800 °C).

For the quantitative confirmation of these findings, further detailed glow discharge optical emission spectroscopy (GDOES) analyses were carried out (as shown in Fig. 4), which demonstrates the quantitative chemical elemental distribution changes across the Pt/TiO<sub>2</sub>/Pt layered structures. The elemental distribution profile carried out for the as-coated Pt/TiO<sub>2</sub>/Pt structures indicates that a highly non-stoichiometric TiO<sub>2-x</sub> layer was deposited near to the BE-interface. In particular in the region of TE, very low Ti vs higher oxygen concentration than stoichiometric TiO<sub>2</sub> were measured, indicating that excess oxygen adsorbed on the surface of the layer as deposition of TiO<sub>2</sub> layer proceeds (Fig. 4b). The elemental distribution of Ti and O of the T600 and T800 samples, on the other hand, remained constant throughout the layer with a near to stoichiometric Ti:O ratio (1:2) (Fig. 4c). However, a substantially different Ti:O ratio in the region neighboring to BE was measured which is estimated around ~0.85:2.15–0.95:2.05 indicating that the oxygen concentration gradient in the as-coated sample holds at BE even after heat-treatment. Lower oxygen concentration at TiO<sub>2</sub> layer near to BE means that a highly defected TiO<sub>2-x</sub> layer (with plenty of oxygen vacancies V<sub>O</sub><sup>2+</sup>) was formed at the TiO<sub>2</sub>/BE interface (i.e. at the beginning of TiO<sub>2</sub>-deposition). On annealing, the depth profile analysis of the samples T600 and T800 showed a TiO<sub>2</sub> composition closer to the stoichiometric ratio but occurrence of inter-diffusion is probably more efficient at the TiO<sub>2</sub>/BE-interface. The formation of non-stoichiometric TiO<sub>2-x</sub> near to the BE is due to

the fact that oxygen is adsorbed through the BE and its diffusion or supply from the substrate is obstructed. While TE benefits from the oxygen from the air that can be diffused and adsorbed through the porous Pt TE. In addition to that, there appears a lengthy inclination in the slope of Pt content at the transition zone of Pt/TiO<sub>2</sub> for T800 samples (see Fig. S4 of SD) indicating the extension of Pt several nm depths into the TiO<sub>2</sub> at the BE interface. This may be either through the occurrence of a Pt/TiO<sub>2</sub> interdiffusion or related to the rough surface finish of Pt at the BE. Similar observations were reported in [16,17], the exact reasons for this need to be further investigated and proven.

#### 4.3. Electrical measurements and gas sensor tests

The experimental current-voltage (I–V) curves indicate hysteresis as shown in Fig. 4. It is reasonable to assume that in dry air the electron transport is dominating leading to the formation of weak ionic conduction channel inside TiO<sub>2</sub> matrix between Pt-electrodes. The formation of such conducting filament has already been reported in comparable systems [18]. Bousoulas et al. [19] proposed that the oxygen vacancies density and distribution in the TiO<sub>2</sub> matrix have a direct impact on the conducting filament diameter, in terms of sensitivity of the conducting paths. High vacancy density results in better switching behavior, but the ultrahigh density of vacancies deteriorate the switching phenomenon.

Moreover, it is likely that the width of ionic conduction channel will be very narrow (a few nm) under air environment. Since the TiO<sub>2</sub> sensing layer is highly reduced at the Pt/BE-interface, the hysteresis obtained for reverse bias will be very low in technical air background (See Fig. 5a,b). However, under H<sub>2</sub> exposure, this hysteresis becomes prominent in both forward and reverse biased conditions, as indicated in Fig. 5c,d. The asymmetrical non-linear characteristics of I–V plots correspond expectedly to the rectifying behaviour (i.e. Schottky interface) of both interfaces (Fig. 5a–d). Generally, for a Pt/TiO<sub>2</sub> interface, a Schottky barrier is formed [20]. Its height ( $\phi_{SB}$ ) can be estimated by using  $\phi_{SB} = \Phi_{Pt} - \chi_{TiO_2}$ , where  $\Phi_{Pt}$  is the work function of Pt and  $\chi_{TiO_2}$  is the electron affinity of TiO<sub>2</sub>. As the standard value of  $\Phi_{Pt}$  is ~5.65 eV [20] and  $\chi_{TiO_2}$  is ~4.16 [21], the equation gives a theoretical Schottky barrier height of 1.44 eV. The height of “Schottky barrier ( $\phi_{SB}$ )” at the TE/TiO<sub>2</sub>-interface is probably higher than that at the TiO<sub>2</sub>/BE-interface. In order to confirm this anticipation, the Schottky barrier ( $\phi_{SB}$ ) heights were calculated with the assumption that the I–V characteristics base on the thermionic field emission conduction mechanism [22] and TiO<sub>2</sub> layers act as intrinsic n-

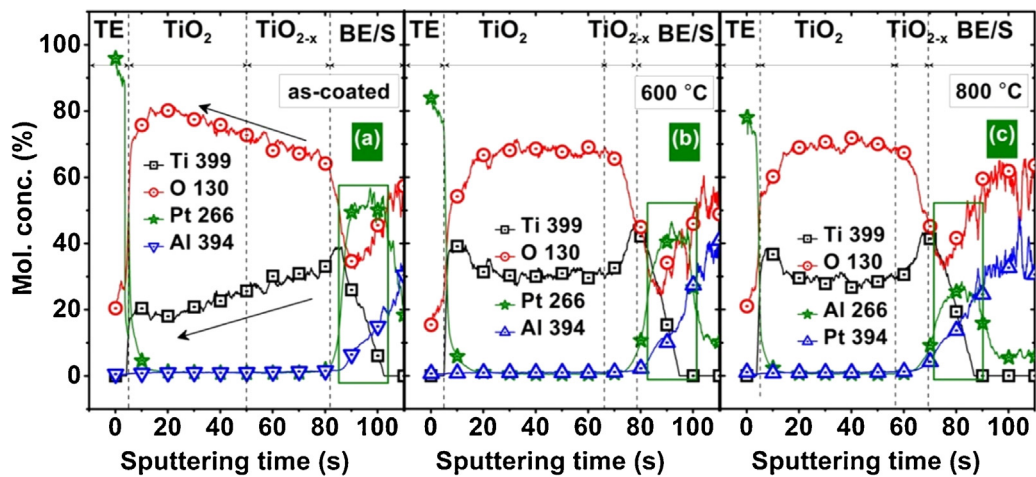


**Fig. 4.** The depth profile of the Pt/TiO<sub>2</sub>/Pt structures, as coated (a), annealed at 600 °C (b) and 800 °C (c) by GDOES analysis. The spectral intensities characteristics of Ti399, O130, Pt266 and Al394 are shown as a function of sputtering time, which corresponds to sputtered depth. Here S indicates the Al<sub>2</sub>O<sub>3</sub> substrate.

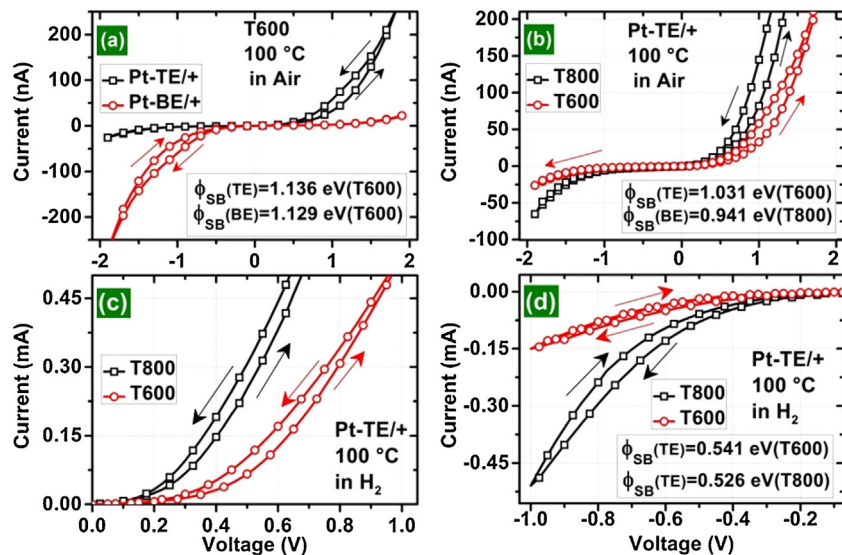


**Fig. 5.** The experimental current–voltage characteristics (I–V) of T600 under both TE+ and BE+ biasing conditions are shown in (a). For the comparison purposes, the current–voltage characteristics (I–V) of both heat-treated samples, T600 and T800 are shown in (b), from –2 to +2 V at 100 °C and a sweep of 100 mV only with TE+ biasing. For clarity, the measurements were carried out at 100 °C because the I–V curves at RT and 50 °C showed background noise due to high resistivity and limitation of the source–meter. Here TE+ represents the measurements with the bias voltage applied to the TE as the BE grounded and the label “BE+” indicate the bias voltage applied to BE as the TE grounded. The calculated Schottky barrier heights ( $\phi_{SB}$ ) for both samples are also indicated. The magnified view of the typical forward and reverse I–V characteristics in 10000 ppm H<sub>2</sub> gas for both samples, T600 and T800 are shown in (c) and (d) respectively. The I–V curves were carried out from –1.0 to +1.0 V, as further increase in the bias voltage could result in the formation of permanent conducting filaments and thus resulting in the low resistance state.

type semiconductor. Thus the calculated Schottky barrier height for the T600 samples at the TE/TiO<sub>2</sub>–interface is ( $\phi_{SB}$  (TE) ~ 1.136 eV) being slightly higher than that at the TiO<sub>2</sub>/BE–interface (e.g.  $\phi_{SB}$  (BE) ~ 1.129 eV). Both values are very close to the theoretically estimated value of 1.44 eV. For the T800 samples, however, the calculated values at both interfaces drop further, becoming significantly low at the TiO<sub>2</sub>/BE–interface ( $\phi_{SB}$  (TE) ~ 1.031 eV >  $\phi_{SB}$  (BE) ~ 0.941 eV). Thus it can be summarized that the Schottky barrier heights at both interfaces of T600 sample are higher than those at the T800 samples; i.e.  $\phi_{SB}$  (TE/TiO<sub>2</sub>@T600) >  $\phi_{SB}$  (TE/TiO<sub>2</sub>@T800) and  $\phi_{SB}$  (TiO<sub>2</sub>/BE@T600) >  $\phi_{SB}$  (TiO<sub>2</sub>/BE@T800).

Furthermore, upon exposure to 10000 ppm hydrogen, the Schottky barrier height reduces significantly at both interfaces of heat-treated samples (e.g., for T600  $\phi_{SB}$  (TE) ~ 0.541 eV (T600) > for T800  $\phi_{SB}$  (TE) ~ 0.526 eV) probably caused by interaction with H<sub>2</sub> (See Fig. 5c,d). As a consequence of Pt reduction on exposure to H<sub>2</sub>, the work function of Pt decreases leading to the dissociation of H<sub>2</sub>

molecules on Pt surface, diffusion through the Schottky barrier and further reaction with pre-adsorbed oxygen on TiO<sub>2</sub> surface under TE. This behaviour is noticeable in Fig. 5c and d through the significant shift to lower potential values at the I–V plots. According to the equation [ $\Delta\phi_{SB} = \phi_{SB}$  (air) –  $\phi_{SB}$  (H<sub>2</sub>)], the height of Schottky barrier at the metal/semiconductor interface changes depending on the gas concentration and became saturated as such that the interface may approach to flat band bending condition when the H<sub>2</sub> concentration exceeds beyond 0.5% [22].

Both sensors showed high and reproducible sensor response to different fixed hydrogen gas concentrations even at room temperature. The stability and reproducibility of the sensors were checked by recording the repeating gas sensing measurements for a specific gas at least twice under the same experimental conditions. Under the dry conditions, the response improved with the increase in operating temperature (Fig. 6a–f). The response appeared to be highly dependent on the bias polarity of Pt/TiO<sub>2</sub>/Pt layered struc-

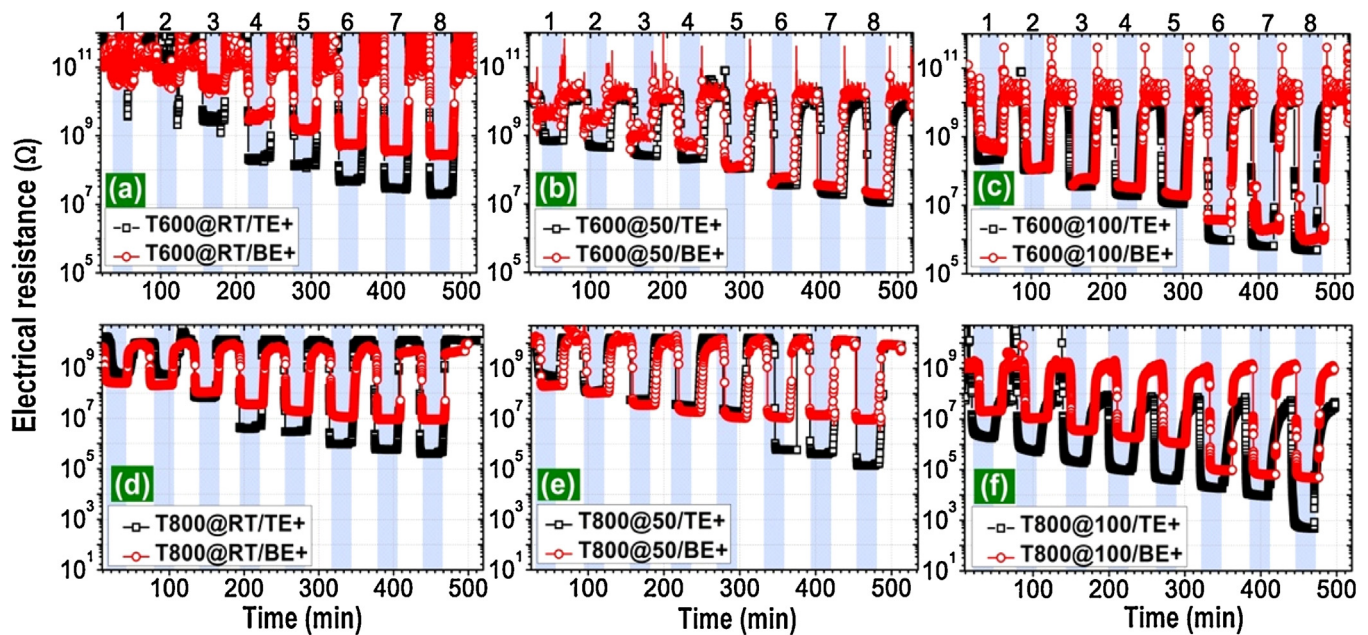


**Fig. 6.** The typical dynamic responses of the sensors T600 (a–c) and T800 (d–f), shows the real-time changes in the electrical resistance upon the gas in/out cycles. The dynamic responses were recorded by using the in-house made software in LabVIEW with a fixed time (30 min) for each gas in/out cycle at room temperature RT (a, d), 50 °C (b, e) and 100 °C (c, f). The responses were measured with an increasing concentration of  $H_2$  gas for each mentioned cycle (1 → 300 ppm, 2 → 500 ppm, 3 → 750 ppm, 4 → 1000 ppm, 5 → 1500 ppm, 6 → 3000 ppm, 7 → 5000 ppm and 8 → 10000 ppm).

ture, i.e. TE+ or BE+. Since the Schottky barrier height for T600 at both interfaces does not vary significantly, the sensor showed overall better response under TE+ biasing conditions (Fig. 6a–c)

For T600 sensor, no response to lower  $H_2$  concentration was seen at room temperature under TE+ biasing most probably due to very high resistance and high Schottky barrier height which limits the transport characteristics. It is also interesting to note that the sensors showed higher response to low concentrations under BE+ biasing and vice versa for TE+ biasing. However, it is crucial to note that this effect became more prominent for T800 samples (Fig. 6d–f). For instance at room temperature the response of T800 sample toward 300 ppm under BE+ biasing is much lower than that for TE+ ( $S_{TE+} \sim 15 < S_{BE+} \sim 50$ ), on the other hand, the sensitivity toward 10000 ppm under TE+, becomes much higher  $S_{TE+} (\sim 1.49 \times 10^6)$  than that under BE+,  $S_{BE+} (\sim 4.10 \times 10^4)$ . In addition, the T800 sample showed lower resistance most probably due to lower Schottky barrier height at Pt-TE/TiO<sub>2</sub> interface. A drift in the sensor signal can be seen for T800 sample under TE+ biased conditions which is likely caused by the partial recovery of the baseline resistance. Otherwise, the transient response remained virtually invariant for both samples to  $H_2$  concentration cycle (the step changes in gas concentrations are labelled e.g. for the first cycle as “1” 0 → 300 ppm → 0).

Fig. 7 shows the sensor response ( $R_0/R_g$ ) which was calculated and plotted against various  $H_2$  concentrations. It can be seen that the T600 sensor response increases almost linearly with the  $H_2$  concentration up to around 1500 ppm and tend to saturate at higher concentrations (Fig. 7a–c), which is in good agreement with previous reports [23]. The sample T800 (Fig. 7d–f) showed the same trend with an improved sensor response. However, the response in this case does not tend to saturate at higher concentrations specifically at 100 °C for TE+ biasing. The resistance change, when drawn on logarithmic scale, followed the power law dependency against the wide range of hydrogen concentrations  $R_0/R_g \sim K_{H_2} C_{H_2}^m$ , where “ $K_{H_2}$ ” is a response constant to  $H_2$  and “ $m$ ” is a coefficient of power law dependence [24]; a typical plot is given in SD Fig. S5.

The response and recovery times as a function of hydrogen concentration  $C_{H_2}$  (ppm) are shown in Fig. 8, indicating from the application point of view acceptable values for each concentration. The response time becomes shorter with increasing  $H_2$  concentrations  $C_{H_2}$ , for instance for T600 under TE+ biasing  $T_{res}$  (s)  $\sim$  101, 94, 50 and 45 for  $C_{H_2}$  (ppm) = 300, 500, 750, and 1000 respectively. While the recovery time becomes longer with increasing  $H_2$  concentration, e.g., for T600 under TE+ biasing  $T_{rec}$  (s) = 80, 90, 105, 108 for  $C_{H_2}$  (ppm) = 300, 500, 750, and 1000 respectively. Here, it is reasonable to consider that the longer recovery times are due to the increased hydrogen diffusion through the TiO<sub>2</sub>-layer and then that at the TE/TiO<sub>2</sub> interface under higher  $H_2$  concentrations resulting in slower desorption processes. The values of both  $T_{res}$  (Fig. 8a,b) and  $T_{rec}$  (Fig. 8c,d) show a saturation trend above a critical  $H_2$  concentration which, in the present case, is found as  $C_{H_2} > 1000$  ppm. Probably promoted by the temperature, the T800 sample shows even shorter  $T_{res}$  and  $T_{rec}$  times, as Table (designated Table ST1) in SD displays. In addition, it must be noted that the estimated values of both  $T_{res}$  and  $T_{rec}$  may not exactly represent the real reaction times because the dynamics of gas-surface interaction or the gas diffusion through the sensing layer are determined by the measurement method as already discussed elsewhere [25].

Although widely used as chemical sensors, the response of MOX-based sensors suffers in the presence of humidity and the operating temperature variations. Humidity may affect the sensor response by suppressing it to lower levels. Thus, environmental humidity and the operating temperature vary significantly over seasons and may lead to the poisoning on the sensor surface. It is mostly believed that this response alteration caused by humidity is due to the substitution of adsorbed oxygen which is present on the MOX surface with hydroxyl groups [26]. Some reports suggest that the poisoning due to humidity can be lowered or reduced to a negligible level by doping the MOX sensing material with suitable, mostly metallic, dopants [27]. However, up to now, there are no reports for a totally stabilized sensor response that is totally independent of the operating temperature.

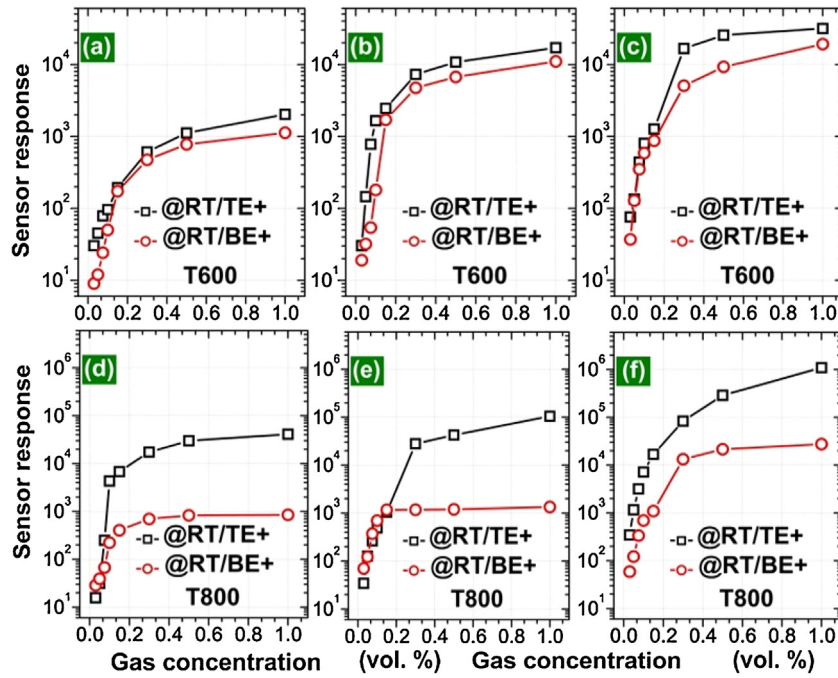


**Fig. 7.** The plots of sensor response ( $S = R_0/R_g$ ) versus increasing hydrogen gas concentrations ( $C_{H_2}$ ) for the sensors annealed at 600 °C (a, b, c) and 800 °C (d–f) were evaluated from transient responses presented in Fig. 6. The sensor responses were calculated from the ratio of base resistance in air ( $R_0$ ) to saturated resistance value ( $R_g$ ) in specific hydrogen concentration ( $C_{H_2} = 300\text{--}10000$  ppm) at RT (a, d), 50 °C (b, e) and 100 °C (c, f).

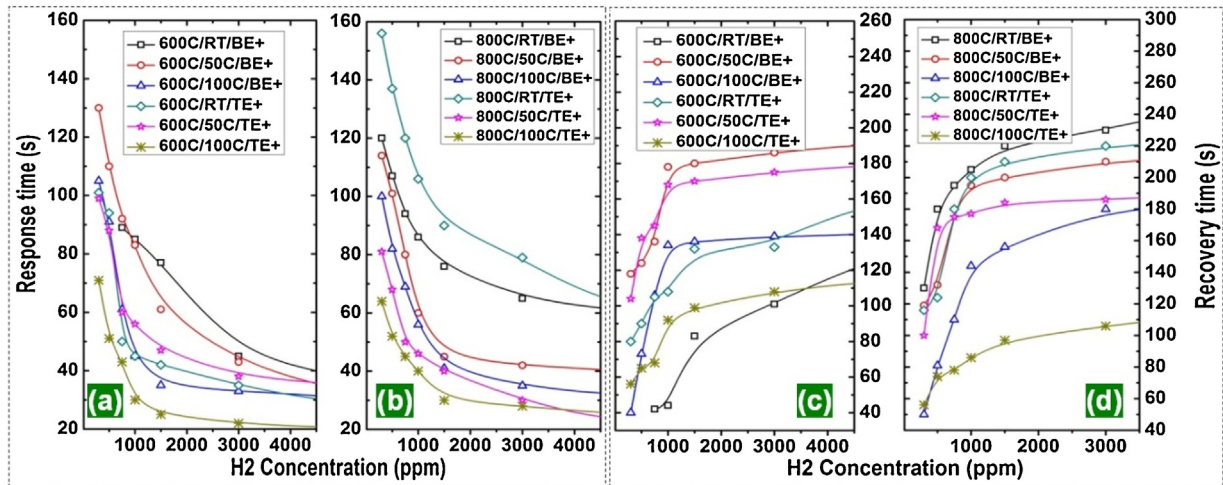


**Fig. 8.** Dependence of response and recovery time against H<sub>2</sub> gas concentrations of T600 sensors (a and c) and T800 sensors (b and d). The response and recovery time were evaluated from transient responses presented in Fig. 6 for the 90% change in the resistance, upon exposure to specific gas concentration, from its original baseline value. The labels on y-axis and x-axis for both response time curves (a and b) and recovery time curves (c and d) are the same.

Hence, this present study investigates the reasons to establish an understanding of hydrogen sensing with Pt/TiO<sub>2</sub>/Pt sensor characteristics under humidity and at different operating temperatures. As expected, the resistance of the sensors decreases in the presence of 50% RH. The results in Fig. 9a,b exhibits that the sensors show better response toward hydrogen under relative humidity (e.g., at RT for T800/TE+ under 10000 ppm H<sub>2</sub> the  $R_0/R_g$  (50% RH)  $\sim 5.3 \times 10^5 \gg R_0/R_g$  (0% RH)  $\sim 2.5 \times 10^4$ ). The response of the sensor is highly dependent on bias polarity in dry air condition, while becomes independent in wet air condition (Fig. 9a). Fig. 9b displays that the same sensor response is to receive in a humid environment at RT, 50 °C and 100 °C when exposed to 10000 ppm hydrogen, indicating temperature independent behaviour of the sensor. Furthermore, it is to note that the reaction and recovery times are reduced from 19 to 3 s and 118 to 9 s respectively at RT,

again toward 10000 ppm (see Fig. 9c,d). In addition, these sensors were also tested for interfering gases CO and NO<sub>2</sub>. As Fig. 9e demonstrates, at RT the sensor response to 200 ppm CO is negligibly small while almost no response to 250 ppm NO<sub>2</sub> can be detected what makes such sensors incredibly suitable for practical applications. To the best knowledge of the authors, there is no literature report on the observation of such sensor characteristics. Table 1 compares the sensor results obtained in this study with those previously reported in the literature.

#### 4.4. Discussion of sensing mechanism

There are two generally accepted and well-established sensing mechanisms for metal oxide based sensors, most commonly using interdigitated electrodes (IDEs). These are ionosorption and

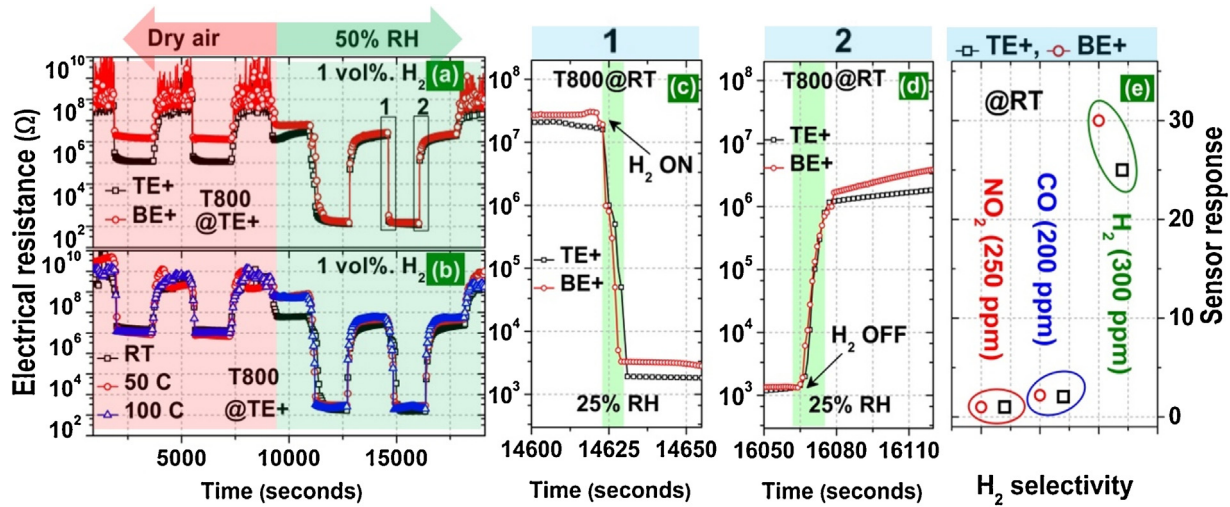
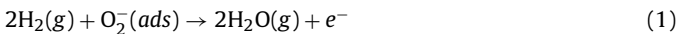


**Fig. 9.** Time-dependent resistance changes of the sensor T800 toward 10000 ppm hydrogen in dry air and under 50% RH at room temperature with applied bias (a) and operating temperature dependency (b). The magnified sensor response from (a) are shown in (c) and (d) to elaborate the fast reaction and recovery time. The hydrogen selectivity of the sensor is shown in (e).

**Table 1**  
Comparison of the current work highlights with previous works.

Sensor system	Background condition	C <sub>H2</sub> (ppm)	T (°C)	Sensor Response	T <sub>res</sub> /T <sub>rec</sub> (s)	Remarks
Pt/TiO <sub>2</sub> /Pt	Dry air	10000	RT	~10 <sup>7</sup>	NR	Top Pt electrode width was of nm scale; selectivity was not reported
Pt/WO <sub>3</sub> /Pt	Humid air	Not Reported (NR)	150	~2 × 10 <sup>3</sup>	22/120	Cr <sub>2</sub> O <sub>3</sub> -sensitivity was not addressed [28]
Au/Pd/TiO <sub>2</sub> /Ti	Dry air	8000	250	2.6 × 10 <sup>3</sup>	27/78	Anodized TiO <sub>2</sub> ; The Res <sub>N2</sub> /Res <sub>Air</sub> method was used to evaluate the sensor response
Au/Pd-Pt/TiO <sub>2</sub> /Ti	Humid air	Not Reported (NR)	RT	3.8 × 10 <sup>3</sup>	41/62	Anodized TiO <sub>2</sub> ; High bias voltage ~ 10 V [10]
Pt/TiO <sub>2</sub> /Ti	Dry air	15	RT	~5	120/-	Anodized TiO <sub>2</sub> ; Dynamic responses missing [11]
Pt/TiO <sub>2</sub> /Ti	Humid air	Not Reported (NR)	RT	3.1 × 10 <sup>3</sup>	80/41	Anodized TiO <sub>2</sub> Nanotubes; selectivity was not reported [30]
Pt/TiO <sub>2</sub> /Ti	Dry air	1000	290	~10 <sup>3</sup>	150	Temperature independent sensitivity under humidity; Low sensitivity to NO <sub>2</sub> and CO [this work]
Pt/TiO <sub>2</sub> /Pt	Humid air	Not Reported (NR)	RT	~5 × 10 <sup>4</sup>	35/180	
Pt/TiO <sub>2</sub> /Pt	Humid air	10000	RT	~6 × 10 <sup>5</sup>	5/11	

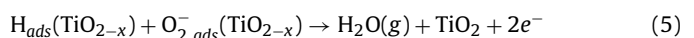
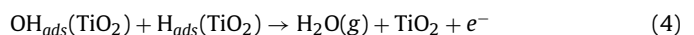
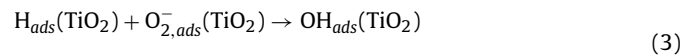
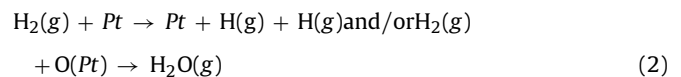
reduction-reoxidation mechanisms. Ionosorption on the n-type metal oxide semiconducting sensing layer surface follows gas adsorption, charge transfer (occurring as a consequence of gas reaction with pre-adsorbed oxygen) and desorption [25–30] as described by the following reaction (Eq. (1)):



The second mechanism (e.g. the so-called reduction-reoxidation model) is based on the surface reduction and reoxidation of the sensing layer under gas exposure [26]. Both mechanisms are however essentially valid for the sensors with interdigitated electrode structure and mainly consider the basic gas reactions occurring on the metal oxide layer surface (such as Eq. (1)) while the changes in sensing layer is explained in general with the variations in the surface depletion layer and intergranular surface potential ( $eV_s$ ).

In turn, the Schottky diode based sensor configuration, i.e. quasi similar to Pt/TiO<sub>2</sub>/Pt sensor structure, the sensing mechanism is primarily justified with the variations in Schottky Barrier Height at the Pt/TiO<sub>2</sub> interface. As a general trend, the resistance of Pt/TiO<sub>2</sub>/Pt structure decreases upon exposure to H<sub>2</sub> as a consequence of the reaction of H<sub>2</sub> with the Pt top electrode (TE) surface (Eq. (2)). Similarly, hydrogen reacts with on TiO<sub>2</sub> surface pre-adsorbed oxy-

gen (Eq. (3)). Following the adsorption and diffusion of hydrogen through the TiO<sub>2</sub>-layer occur (Eq. (3)) yielding a significant increase of charge carrier concentration  $e^-$  below the TE interface (Eqs. (4) and (5)) and creating a gradient of point defect density through the sensing layer generated by the applied bias field. These reactions and the related charge carrier transfer and ionic channel formation are illustrated in Fig. 10.



Recently, a combinational hydrogen sensing mechanism for Pt-TiO<sub>2</sub>-Pt sensor structure has been suggested on the basis of hydrogen diffusion related resistivity changes in TiO<sub>2</sub> layer and hot electron emission related to high electric field [9]. Neverthe-

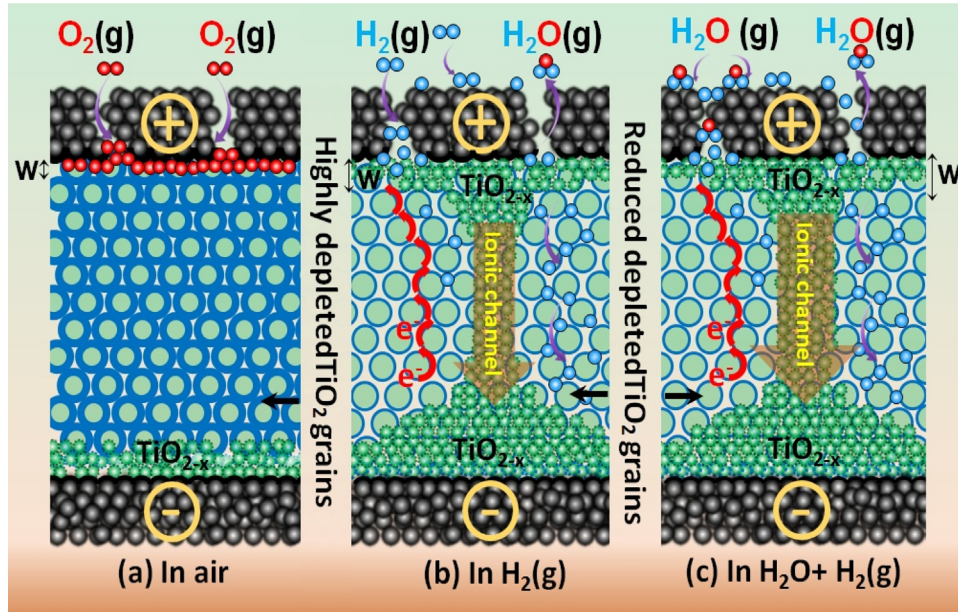


**Fig. 10.** Illustration of sensing mechanism with Pt/TiO<sub>2</sub>/Pt structure shows the diffusion of oxygen molecules/ions (●●) through Pt-TE with pores structure, creating a depletion region on TiO<sub>2</sub> (●) atoms (a). The hydrogen gas (●●) reaction at TE, dissociation into H<sup>+</sup> (●) and further diffusion into the bulk TiO<sub>2</sub> by forming an ionic filament with arrow pointing its direction under TE+ biasing condition is shown in (b). The hydrogen sensing mechanism and broadening of ionic filament channel width under humid environment are shown in (c). Here e<sup>-</sup> represents electrons and their conduction with arrow (curved red) indicates the drift/movement towards positive biasing through TiO<sub>2</sub> grain boundaries with less depletion region. (For interpretation of the references to colour in this figure legend, the reader is referred to the web version of this article.)

less, up to now, it has not been clearly defined to what extent such processes occur, what are the consequences of hydrogen diffusion through the sensing layer and more importantly what is the origin of high hydrogen sensitivity. Furthermore, the complex phenomenon related to the effects of humidity during room temperature hydrogen sensing with M/MOX/M sensor structure (M=metal) has been left undiscussed.

The novelty in this context thus is the proposed sensing mechanism elucidated on the basis of above presented experimental results including humidity effect. The model sketched in Fig. 10 demonstrates the formation of ionic conduction channel along with electron conduction path being in the opposite direction. Initially, electron diffusion dominates the overall conduction and, under air background, the ionic conduction is very weak represented with a narrow width, analogue to the high resistance state of a memristor [31]. This initial stage is also evident from the I–V curves given in Fig. 4a,b. However, the width of this ion channel becomes wider under hydrogen exposure caused by high resistance change [31], as a similar way observed with the low resistance state of memristor (Fig. 10a–c).

This model puts forward that the total resistance of the sensor is the sum of the contributions from the Pt/TiO<sub>2</sub> interface condition, electronic conduction and ionic conduction as the following Eq. (6) outlines the merge of these contributions:

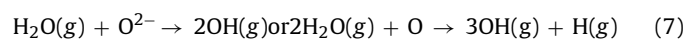
$$R_{total} \cong A \exp\left(\frac{\phi_{SB}}{k_B T}\right) + \left[\frac{1}{|e|\mu_e[e^-]}\right] \exp\left(\frac{eV_s}{k_B T}\right) + \left[\frac{1}{w|e|\mu_v[V_O^{**}][O_i]}\right] \exp\left(\frac{E}{k_B T}\right) \quad (6)$$

The contributions from the Pt electrode/sensing layer interface depend, in addition to temperature, on the contact area ( $A$  in Eq. (6) is a constant related to contact dimension) and on Schottky Barrier Height. While the electronic contribution depends on electron mobility  $\mu_e$ , number of free electrons  $[e^-]$  and intergranular surface potential  $eV_s$ . The ionic conduction part of the resistance plays an

additional dominating role in high resistance change driven with hydrogen (will be discussed later), which depends on a number of variations, such as the width of reduced auto-doped TiO<sub>2-x</sub> layer near the top electrode  $w$  (see Fig. 10b,c), applied electric field  $E$ , ionic mobility  $\mu_v$ , number of oxygen vacancies  $[V_O^{**}]$  and ions  $[O_i]$ . Here  $k_B$  is the Boltzmann constant and  $T$  is the absolute temperature.

As established with observations, under air exposure, the width of the reduced TiO<sub>2-x</sub> at TE is negligible and maintained constant along TE. In turn, hydrogen reaction on TiO<sub>2</sub> surface near TE results in the formation oxygen vacancies as well as oxygen ions causing an increase of reduced TiO<sub>2-x</sub> top layer rapidly. Meanwhile, the width of the reduced TiO<sub>2-x</sub> at the BE-side will be maintained quasi-constant in air as well as hydrogen. Thus, it is reasonable to believe that the self-generation of such double layer will cause a rapid resistance change, although with the applied voltage (i.e. 1 V) generated electric field will remain constant throughout the layer. The high mobility of electron transport  $\mu_e \sim 25 \text{ cm}^2/\text{Vs}$  through the sensing layer on the other hand causes in a rapid reduction of sensor's resistance under hydrogen, hence resulting in the shortening of reaction/recovery times. In contrast, hydrogen sensing in humid environment is stabilized or enhanced due to the surface adsorption of hydrogen on Pt and further migration of H<sub>2</sub>O species (monomers, dimers, trimers or clusters) towards pre-adsorbed oxygen.

The surface reaction of water vapor on Pt is controversial. Some authors [32,33] reckon that water vapors may dissociate into hydroxyl groups on Pt surface and further migrate to the sensing layer. Contrary, assumption to that given by the excellent and authenticated reviews of M. A. Henderson and U. Diebold [34,35], acclaiming that the water molecules do not dissociate on Pt surface, instead, they are adsorbed on Pt surface to yield mono- or multi-layers and further diffusing into the sensing layer. After diffusion from Pt top electrode, the water being in gas-phase reacts with pre-adsorbed oxygen over a gas-phase route [32–35]:



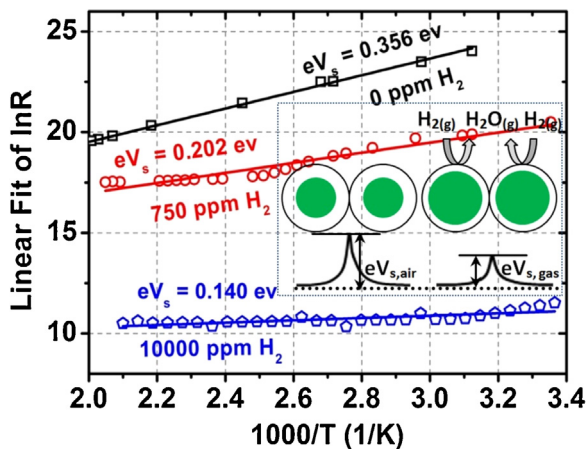


**Fig. 11.** The Arrhenius plots for T800 sample derived from resistance versus operating temperature (RT – 200 °C) measured in technical air, 750 ppm and 10000 ppm H<sub>2</sub> environment. The symbols indicate the original data and line indicate the linear fit. The value of  $eV_s$  (eV) was obtained from the slope of the linear fit and we assume it to be equal to intergranular surface potential barrier height originated between the grains ( $R_{air} = R_0 \exp(eV_{s,Grain}/k_B T)$ ) as indicated in the inset. Here  $k_B$  is the Boltzmann constant and  $T$  is the absolute temperature.

M. A. Anderson and U. Diebold [33,34] present in their review articles the detailed surveys of previous work about water adsorption on metal surfaces (such as that on Pt (111) surface) as well as the surface science of TiO<sub>2</sub> related issues. For further information, the reader is referred to these articles. Water dissociation process at TiO<sub>2</sub> surface occurring on reaction with pre-adsorbed oxygen leads to the release of by surface oxygen captured electrons e<sup>-</sup>. But extend of this process is evidently limited at the Pt-TE-interface due to the less surface step coverage of H<sub>2</sub>O (g) as displayed in Fig. 8, where a scarce resistance change is observed under 50% RH at RT. It is likely that in the presence of H<sub>2</sub>O, the dissociation process creates temporary dipole formation only a few nm beneath the Pt-TE and leads to the generation of hydronium ions:



Subsequently, under hydrogen exposure, the reaction of hydrogen with the adsorbed H<sub>2</sub>O vapors takes place generating H<sup>+</sup>(g) and releasing electrons as suggested by Anderson. Consequently, these generated high numbered H<sup>+</sup>(g) ions drift swiftly and break the dipole by reacting with oxygen sites. Thus a large number of oxygen vacancies are created below Pt-TE which drift quickly towards negative biased terminal of the sensor and thus cause in a widening of the reduced TiO<sub>2-x</sub> (Fig. 9c). Under TE+ condition then, the electrons drift away from the BE as the oxygen ions O<sub>i</sub> and vacancies V<sub>O</sub><sup>••</sup> (produced during H<sub>2</sub> exposure) drift toward the negatively biased electrode TE- yielding a significant reduction in the resistance. In addition, through the H<sub>2</sub> interaction with the surface as well as within the sensing layer, the depletion layer grows thinner, and as result, the intergranular surface potential ( $eV_s$ ) decreases providing a convenient path for electron transfer and electrical transport. Hence, H<sub>2</sub> exposure caused overall resistance decrease is controlled by combined variations of (i) intergranular surface potential ( $\Delta eV_s$ ), (ii) interfacial Schottky barrier height ( $\Delta \phi_{SB}$ ) and (iii) the width of reduced TiO<sub>2-x</sub> at the TE. On the other hand, thickness reduction of the reduced TiO<sub>2-x</sub> zone near the sensing surface plays a dominating role in the sensing mechanism due to the generation of oxygen vacancies and drift of ions towards negative terminal. This hypothesis is supported by the temperature dependent resistance measurements given in Fig. 11 which yield the estimated intergranular surface potential  $eV_s$ . The value of  $eV_s \sim 0.356$  eV in air is comparatively smaller than the interfacial Schottky barrier height in air at both interfaces [TE/TiO<sub>2</sub> ( $\phi_{SB}(TE) \sim 1.031$  eV

or TiO<sub>2</sub>/BE ( $\phi_{SB}(BE) \sim 0.941$  eV]. This obtained result is reasonable and comparable to those previously reported [19,20]. The relatively high Schottky Barrier Height additionally confirms that through the applied voltage generated electric field is not homogenously distributed in air along the sensing layer. The smaller value of intergranular surface potential  $eV_s$  also indicates that the grains are depleted due to low surface charge carrier concentration [e<sup>-</sup>] captured by pre-adsorbed oxygen.

Additionally, it is to note that, after H<sub>2</sub> gas exposure, the change in intergranular surface potential ( $eV_{s,air} - eV_{s,1\%H_2} \sim 0.356 - 0.140 \sim 0.216$  eV) as well as Schottky Barrier Height (for T800  $\Delta \phi_{SB} \sim 0.42$ ) are comparatively small considering such high resistance changes. Thus it is logical that the change in near surface reduce width (w) play the significant role. It is most probable that all three resistance changes co-exist as one of them becomes dominant at a particular given situation. For instant, it can be speculated that Schottky Barrier variation plays dominant role as a result of biasing condition, (see Figs. 7 and 8). At higher H<sub>2</sub> concentrations ( $C_{H_2} > 1000$  ppm), both sensors (T600 and T800) show better responses under TE+ biasing condition than TE- and vice versa is true for lower concentrations. The resistance of both sensors in hydrogen ( $R_{gas}$ ) decreases first due to the decrease in surface potential  $eV_s$  and then becomes saturated. In this saturation period, a further decrease occurs in resistance and electronic transport depending on the height of Schottky Barrier  $\phi_{SB}$  and the drift condition of oxygen vacancies. For smaller H<sub>2</sub> concentrations, the electrical transport is basically governed by the number of free charge carriers, i.e. electrons. In turn, particularly for higher H<sub>2</sub> concentrations, it is to expect that the main source of sensing mechanism is due to the temperature induced variations in the reduced TiO<sub>2-x</sub> surface layer while those are temperature independent yielding high sensor response under humid environment.

Nevertheless, the scientific explanation of such high sensitivity is still debated and the models require confirmation by in-situ spectroscopic analysis (such as XPS) to determine the dependency of variation of such reduced TiO<sub>2-x</sub> phases with hydrogen and water vapor. We suggest for example that Magneli phases Ti<sub>n</sub>O<sub>2n-1</sub> may form in a reduced environment due to oxygen ions and the drift of vacancies. However, it is worthwhile noticing that such phases may have an intermediate character under gas exposure and may disappear on cease of gas. Further thorough analyses are needed to clear this and other similar questions which extend out of the scope of this paper.

## 5. Conclusion

A Pt/TiO<sub>2</sub>/Pt gas sensor configuration was designed and implemented for the detection of hydrogen. An inter-diffusion at both interfaces Pt-TE/TiO<sub>2</sub> and TiO<sub>2</sub>/Pt-BE is observed by EDX with more Pt diffusing into the TiO<sub>2</sub> layer at the BE-side. This observation is confirmed further by GDOES analysis and current-voltage characteristics. The sensors show promising hydrogen gas sensing properties even under relatively low H<sub>2</sub> concentrations (e.g. 700 ppm) at room temperature. Under humid environment, the sensing properties are enhanced and the sensors show temperature independent hydrogen sensitivity. The response and recovery times are only 5 and 9 s respectively for 1% H<sub>2</sub> in 50% RT (relative humidity). The sensing mechanism is discussed and explained basing on three variations present in the sensor structure: (i) intergranular surface potential ( $\Delta eV_s$ ), (ii) interfacial Schottky Barrier Height ( $\Delta \phi_{SB}$ ) and (iii) the depth of reduced TiO<sub>2-x</sub> zone at the TE. It is proposed that although all three variations may be present in these sensor structures, only one of these factors will play the dominant role which is defined individually by each physical sit-

uation. For instance, it is observed that the sensors show good response under BE+ biasing to low hydrogen concentrations, and in turn, under TE+ biasing to high concentrations. Such effects appear to be dependent on the Schottky Barrier Height at TE. On the other hand, intergranular surface potential variations and the resistance of sensing layer which saturates under H<sub>2</sub> due to changes in the depletion layer determine the drift of oxygen vacancies or free charge carrier transport and the resulting sensitivity is higher.

In summary, it is believed that the overall sensing mechanism is controlled by the variation of the auto-doped reduced TiO<sub>2-x</sub> layer near the TE. Future work has to be performed to see the effect of ohmic interface and highly reduced TiO<sub>2</sub> surface as well as bulk, the optimisation of which will definitely result in exceptional gas sensing properties.

## Acknowledgements

The authors acknowledge the support provided by DAAD and DLR under DAAD-DLR Fellowship number 165. The valuable support and comments from Prof. Dr. Uwe Schulz is highly appreciated. The authors thank Prof. Dr. Klaus Schierbaum from university of Dusseldorf for his discussion about sensing mechanism. The authors thank Mr. Jorg Brien, Mr. Andreas Handwerk and Daniel Peters of DLR-WF for the synthesis of sensing and electrode layers. Dr. Azhar Ali Haidry thank Prof. Zhengjun Yao dean of MSC-NUAA for his support during the write up of this manuscript. Dr. Azhar Ali Haidry also thank Ms. Qawareer Fatima (MSc student at MSC-NUAA) for her assistance in data analysis.

## Appendix A. Supplementary data

Supplementary data associated with this article can be found, in the online version, at <http://dx.doi.org/10.1016/j.snb.2017.06.159>.

## References

- [1] K. Mazloomi, C. Gomes, Hydrogen as an energy carrier: prospects and challenges, *Renew. Sustain. Energy Rev.* 16 (2012) 3024–3033, <http://dx.doi.org/10.1016/j.rser.2012.02.028>.
- [2] S. Singh, S. Jain, P.S. Venkateswaran, A.K. Tiwari, M.R. Nouni, J.K. Pandey, S. Goel, Hydrogen: a sustainable fuel for future of the transport sector, *Renew. Sustain. Energy Rev.* 51 (2015) 623–633, <http://dx.doi.org/10.1016/j.rser.2015.06.040>.
- [3] M. Nasir Uddin, W.M.A.W. Daud, H.F. Abbas, Potential hydrogen and non-condensable gases production from biomass pyrolysis: insights into the process variables, *Renew. Sustain. Energy Rev.* 27 (2013) 204–224, <http://dx.doi.org/10.1016/j.rser.2013.06.031>.
- [4] T. Hübert, L. Boon-Brett, G. Black, U. Banach, Hydrogen sensors—a review, *Sens. Actuators: B Chem.* 157 (October (2)) (2011) 329–352, <http://dx.doi.org/10.1016/j.snb.2011.04.070>.
- [5] J.W. Buttner, M.B. Post, R. Burgess, C. Rivkin, An overview of hydrogen safety sensors and requirements, *Int. J. Hydrogen Energy* 36 (February (3)) (2011) 2462–2470, <http://dx.doi.org/10.1016/j.ijhydene.2010.04.176>.
- [6] S.K. Arya, S. Krishnan, H. Silva, S. Jean, S. Bhansali, Critical review: advances in materials for room temperature hydrogen sensors, *Analyst* 137 (2012) 2743.
- [7] S. Vallejos, I. Gracia, O. Chmella, E. Figueras, J. Hubalek, C. Cane, Chemoresistive micromachined gas sensors based on functionalized metal oxide nanowires: performance and reliability, *Sens. Actuators B* 235 (2016) 525–534, <http://dx.doi.org/10.1016/j.snb.2016.05.102>.
- [8] A. Renitta, K. Vijayalakshmi, Highly sensitive hydrogen safety sensor based on Cr incorporated ZnO nano-whiskers array fabricated on ITO substrate, *Sens. Actuators B* 237 (2016) 912–923, <http://dx.doi.org/10.1016/j.snb.2016.07.017>.
- [9] T. Plecenik, M. Mosko, A.A. Haidry, P. Durina, M. Truchly, B. Grancic, M. Gregor, T. Roch, L. Satrapinsky, A. Moskova, M. Mikula, P. Kus, A. Plecenik, Fast highly-sensitive room-temperature semiconductor gas sensor based on the nanoscale Pt–TiO<sub>2</sub>–Pt sandwich, *Sens. Actuators B* 207 (2015) 351–361, <http://dx.doi.org/10.1016/j.snb.2014.10.003>.
- [10] M. Strungaru, M. Cerchez, S. Herberitz, T. Heinzel, M. El Achhab, K. Schierbaum, Interdependence of electroforming and hydrogen incorporation in nanoporous titanium dioxide, *Appl. Phys. Lett.* 106 (2015) 143109, <http://dx.doi.org/10.1063/1.4917034>.
- [11] M. Cerchez, H. Langer, M.E. Achhab, T. Heinzel, H. Lüder, D. Ostermann, Dynamics of hydrogen sensing with Pt/TiO<sub>2</sub> Schottky diodes, *Appl. Phys. Lett.* 103 (2013) 033522, <http://dx.doi.org/10.1063/1.4816265>.
- [12] A.A. Haidry, N. Kind, B. Saruhan, Investigating the influence of Al-doping and background humidity on NO<sub>2</sub> sensing characteristics of magnetron-sputtered SnO<sub>2</sub> sensors, *J. Sens. Sens. Syst.* 4 (2015) 271–280, <http://dx.doi.org/10.5194/jsss-4-271-2015>.
- [13] D.A. Hanaor, C.C. Sorrell, Review of the anatase to rutile phase transformation, *J. Mater. Sci.* 46 (2011) 855–874, <http://dx.doi.org/10.1007/s10853-010-5113-0>.
- [14] Gregory A. Hope, Allen J. Bard, Platinum/titanium dioxide (Rutile) interface: formation of ohmic and rectifying junctions, *J. Phys. Chem.* 87 (1983) 1979–1984, <http://dx.doi.org/10.1021/j100234a029>.
- [15] R.A. Spurr, H. Myers, Quantitative analysis of anatase–Rutile mixtures with an X-ray diffractometer, *Anal. Chem.* 29 (1957) 760–762, <http://dx.doi.org/10.1021/ac60125a006>.
- [16] D. Carta, I. Salaoru, A. Khiat, A. Regoutz, C. Mitterbauer, N.M. Harrison, T. Prodromakis, Investigation of the switching mechanism in TiO<sub>2</sub>-Based RRAM: a two-dimensional EDX approach, *ACS Appl. Mater. Interfaces* 8 (2016) 19605–19611, <http://dx.doi.org/10.1021/acsami.6b04919>.
- [17] A.A. Haidry, C. Cetin, K.B. Saruhan, Sensing mechanism of NO<sub>2</sub> sensing with top-bottom electrode (TBE) configuration, *Sens. Actuators B* 236 (2016) 874–884, <http://dx.doi.org/10.1016/j.snb.2016.03.016>.
- [18] X. Ma, Y. Dai, L. Yu, B. Huang, Interface Schottky barrier engineering via strain in metal-semiconductor composites, *Nanoscale* 8 (2016) 1352–1359, <http://dx.doi.org/10.1039/c5nr05583k>.
- [19] P. Bousoulas, I. Michelakaki, D. Tsoukalas, Influence of oxygen content of room temperature TiO<sub>2</sub>-x deposited films for enhanced resistive switching memory performance, *J. Appl. Phys.* 115 (2014) 034516.
- [20] Matthew T. McDowell, Michael F. Lichterman, Azhar I. Carim, Rui Liu, Shu Hu, Bruce S. Brunschwig, Nathan S. Lewis, The influence of structure and processing on the behavior of TiO<sub>2</sub> protective layers for stabilization of n-Si/TiO<sub>2</sub>/Ni photoanodes for water oxidation, *ACS Appl. Mater. Interfaces* 7 (2015) 15189–15199, <http://dx.doi.org/10.1021/acsami.5b00379>.
- [21] S. Kandasamy, A. Trinchi, M.K. Ghantasala, G.F. Peaslee, A. Holland, W. Wlodarski, E. Comini, Characterization and testing of Pt/TiO<sub>2</sub>/SiC thin film layered structure for gas sensing, *Thin Solid Films* 542 (2013) 404–408, <http://dx.doi.org/10.1016/j.tsf.2013.06.096>.
- [22] V.N. Mishra, R.P. Agarwal, Sensitivity, response and recovery time of SnO<sub>2</sub> based thick-film sensor array for H<sub>2</sub>, CO, CH<sub>4</sub> and LPG, *Microelectron. J.* 29 (1998) 861–874, [http://dx.doi.org/10.1016/S0026-2692\(98\)00019-6](http://dx.doi.org/10.1016/S0026-2692(98)00019-6).
- [23] B. Lyson-Sypien, A. Czaplá, M. Lubecka, P. Gwizdz, K. Schneider, K. Zakrzewska, K. Michalow, T. Graule, A. Reszka, M. Rekas, A. Lacz, M. Radecka, Nanopowders of chromium doped TiO<sub>2</sub> for gas sensors, *Sens. Actuators B* 175 (2012) 163–172, <http://dx.doi.org/10.1016/j.snb.2012.02.051>.
- [24] N. Yamazoe, K. Shimanoe, Theory of power laws for semiconductor gas sensors, *Sens. Actuators B* 128 (2008) 566–573, <http://dx.doi.org/10.1016/j.snb.2007.07.036>.
- [25] A.A. Haidry, et al., Hydrogen gas sensors based on nanocrystalline TiO<sub>2</sub> thin films, *Cent. Eur. J. Phys.* 9 (2011) 1351–1356, <http://dx.doi.org/10.2478/s11534-011-0042-3>.
- [26] A. Gurlo, R. Riedel, In situ and operando spectroscopy for assessing mechanisms of gas sensing, *Angew. Chem. Int. Ed.* 46 (2007) 3826–3848, <http://dx.doi.org/10.1002/anie.200602597>.
- [27] N. Barsan, U. Weimer, Conduction model of metal oxide gas sensors, *J. Electroceram.* 7 (2001) 143–167, <http://dx.doi.org/10.1023/A:1014405811371>.
- [28] Y. Ishikawa, K. Hara, Thin-film gas sensors operating in a perpendicular current mode, *Sens. Actuators B* 181 (2013) 932–937, <http://dx.doi.org/10.1016/j.snb.2013.02.069>.
- [29] T. Hyodo, T. Yamashita, Y. Shimizu, Effects of surface modification of noble-metal sensing electrodes with Au on the hydrogen-sensing properties of diode-type gas sensors employing an anodized titania film, *Sens. Actuators B* 207 (2015) 105–116, <http://dx.doi.org/10.1016/j.snb.2014.10.005>.
- [30] O.K. Varghese, D. Gong, M. Paulose, K.G. Ong, C.A. Grimes, Hydrogen sensing using titania nanotubes, *Sens. Actuators B* 93 (2003) 338–344, [http://dx.doi.org/10.1016/S0925-4005\(03\)00222-3](http://dx.doi.org/10.1016/S0925-4005(03)00222-3).
- [31] J. Joshua Yang, Matthew D. Pickett, Xuema Li, Douglas A.A. Ohlberg, Duncan R. Stewart, R. Stanley Williams, Memristive switching mechanism for metal/oxide/metal nanodevices, *Nat. Nanotechnol.* 3 (2008) 429–433, <http://dx.doi.org/10.1038/nnano.2008.160>.
- [32] T. Lei, S. Zhang, D. Li, D. Lia, W. Zhanga, S. Huanga, C. Xieb, The influence of Au and Pt electrodes on the stability of TiO<sub>2</sub> under UV light activation for sensing formaldehyde in moisture circumstances, *Sens. Actuators B: Chem.* 199 (2014) 15–21, <http://dx.doi.org/10.1016/j.snb.2014.03.094>.
- [33] G. Yamamoto, T. Yamashita, K. Matsuo, Y. Shimizu, Effects of polytetrafluoroethylene or polyimide coating on H<sub>2</sub> sensing properties of anodized TiO<sub>2</sub> films equipped with Pd–Pt electrodes, *Sens. Actuators B* 183 (2013) 253–264, <http://dx.doi.org/10.1016/j.snb.2013.03.136>.
- [34] M.A. Henderson, The interaction of water with solid surfaces: fundamental aspects revisited, *Surf. Sci. Rep.* 46 (2002) 1–308, [http://dx.doi.org/10.1016/S0167-5729\(01\)00020-6](http://dx.doi.org/10.1016/S0167-5729(01)00020-6).
- [35] U. Diebold, The surface science of titanium dioxide, *Surf. Sci. Rep.* 48 (2003) 53–229, [http://dx.doi.org/10.1016/S0167-5729\(02\)00100-0](http://dx.doi.org/10.1016/S0167-5729(02)00100-0).

## Biographies



**Azhar Ali Haidry** received his Bachelor and Master Degrees from Bahauddin Zakariya University (BZU) Multan, Pakistan. From 2004–2008, he taught Physics at BZU and Virtual University (VU) of Pakistan. He carried out his PhD-study during 09.2009–05.2013 under the supervision of Prof. Dr. Andrej Plecenik at Comenius University Bratislava in Slovakia on “micro- to nano-scaled metal oxide gas sensors”. During 08.2013–03.2016, he worked as a Post-Doc at the Institute of Materials Research of the German Aerospace Center (DLR) on semiconductor based gas sensors. Currently, Dr. Haidry is working as Associate Professor at College of Materials Science and Technology, Nanjing University of Aeronautics and Astronautics

(NUAA). His research interests are in the field of nanotechnology, functional coatings, material characterization, metal oxide, chemical sensors and scanning electron microscopy.

**Andrea Ebach-Stahl** is a scientific staff of the Department of High-Temperature and Functional Coatings at the Institute of Materials Research of the German Aerospace Center (DLR) in Cologne/Germany where she is employed since 2005 on her graduation from the Applied University of South Westphalian Iserlohn/Germany. The

main focus area of her study was Surface Science and Nanotechnology. She is the specialist at the department for the physical characterization of thermal-barrier and functional coatings. In 2010, she won the science price of DLR with her publication on protective coatings for TiAl-alloys. Ms. Ebach-Stahl has authored/co-authored up-to-now 20 publications.



**Bilge Saruhan** is a materials scientist with PhD degree on advanced ceramic materials from the University of Limerick/Ireland and lecturing qualification (Habilitation) on nanostructured functional materials and composites from the Technical University of Freiberg/Germany. She received her BSc from the Dept. of Materials and Metallurgical Engineering of Istanbul Technical University (ITU) and her MSc in Materials Science from the Faculty of Chemistry and Metallurgy of ITU. Since completing her PhD, she has been working at the Institute of Materials Research of the German Aerospace Center (DLR) in Cologne/Germany where she presently leads the activities on functional coatings with emphasis on sensors and battery-like supercapacitor electrodes. Her research interests cover ceramic matrix composites, thermal barrier coatings, gas sensors, catalytic materials and energy storage materials. Up to date, she has authored/co-authored 112 papers, published 1 book and holds 7 (3 pending) patents.